Amplification of photoacoustic effect in bimodal polymer particles by self-quenching of indocyanine green

MAKSIM D. MOKROUSOV,[1] **MARINA V. NOVOSELOVA,**[1] **JACKIE NOLAN,**[2] **WALTER HARRINGTON,**[2] **POLINA RUDAKOVSKAYA,**[1] **DANIIL N. BRATASHOV,**[3] **EKATERINA I. GALANZHA,**[2,3] **JUAN PABLO FUENZALIDA-WERNER,**[4] **BORIS P. YAKIMOV,**[5] **GLEB NAZARIKOV,**[1] **VLADIMIR P. DRACHEV,**[1,6] **EVGENY A. SHIRSHIN,**[5,7] **VASILIS NTZIACHRISTOS,**[4,8] **ANDRE C. STIEL,**[4] **VLADIMIR P. ZHAROV,**[2,3,9] **AND DMITRY A. GORIN**[1,10]

[1]*Skolkovo Institute of Science and Technology, 3 Nobelya Str, Moscow, 121205, Russia*
[2]*University of Arkansas for Medical Sciences, 4301 W. Markham St. Little Rock, AR 72205, USA*
[3]*Saratov State University, 83 Astrakhanskaya Str, Saratov, 410012, Russia*
[4]*Institute of Biological and Medical Imaging (IBMI), Helmholtz Zentrum München, Neuherberg, Germany*
[5]*Lomonosov Moscow State University, Leninskie gory 1/2, 119991, Moscow, Russia*
[6]*University of North Texas, 1155 Union Circle, Denton, TX 76203, USA*
[7]*Institute of Spectroscopy of the Russian Academy of Sciences, Fizicheskaya Str., 5, 108840, Troitsk, Moscow, Russia*
[8]*Chair of Biological Imaging and Center for Translational Cancer Research (TranslaTUM), Technische Universität München, Munich, Germany*
[9]*zharovvladimirp@uams.edu*
[10]*d.gorin@skoltech.ru*

Abstract: A new type of bimodal contrast agent was made that is based on the self-quenching of indocyanine green (ICG) encapsulated in a biocompatible and biodegradable polymer shell. The increasing of a local ICG concentration that is necessary for the obtaining of self-quenching effect was achieved by freezing-induced loading and layer-by-layer assembly. As a result, an efficient photoacoustic(optoacoustic)/fluorescent contrast agent based on composite indocyanine green/polymer particles was successfully prepared and was characterized by fluorescence and photoacoustic(optoacoustic) tomography *in vitro*. This type of contrast agent holds good promise for clinical application owing to its high efficiency and biosafety.

1. Introduction

Many imaging modalities have been used in preclinical and clinical studies, including magnetic resonance imaging (MRI) [1], photoacoustic (PA) tomography (PAT) [2], ultrasound [3], positron-emission tomography (PET) [4], single-photon emission computed tomography (SPET) [5], fluorescence tomography (FT) [6], and optical coherence tomography (OCT) [7]. Fluorescence and photoacoustic(optoacoustic) tomography have acceptable levels of all parameters for both clinical and preclinical applications. The most important parameters include deep penetration into tissue (several centimetres), good spatial resolution (up to microns), and very high sensitivity to contrast agents at the level of nanomoles per litre [8]. The ability to have bimodal contrast decreases the number of artefacts during *in vivo* imaging and abates subsequent problems with image processing for diagnostic purposes. Nowadays, there is a list of requirements for contrast agents. The most important ones are the lower limit of quantification (LLOQ), linear concentration dependence, high selectivity, biocompatibility, biodegradability, and multimodality.

Multimodality is a key parameter for verification and validation of signal reliability. It is well known that the photoacoustic signal is proportional to 1 minus fluorescence quantum yield; therefore, with a dye, it is difficult to obtain both high fluorescence and high photoacoustic signals. A possible solution is to control the fluorescence intensity by changing the distance between the dye molecule and the plasmon resonant particle surface [9–13]. The distance can be controlled with nanoscale accuracy by using layer-by-layer (LbL) assembled coatings [13] and Langmuir–Blodgett films [14,15] changing the number of layers of the shell between the particle surface and the layer of dye. Varying the distance between the fluorescent dye and the plasmon resonant particle surface can increase the fluorescence intensity and decrease the photoacoustic signal, or it can also lead to fluorescence quenching and, as a result, to an increase in the photoacoustic signal [16]. Another possibility to control the photoacoustic and fluorescence signals is based on the quenching of the fluorescence signal close to the surface of magnetite nanoparticles [17]. Both approaches have a major disadvantage — the presence of inorganic nanoparticles in the nanostructured contrast agents. There are many examples of clinical applications of inorganic nanoparticles or of their combination with organic dyes, used to obtain high extinction or high fluorescence signals. However, using inorganic nanoparticles as a part of contrast agents increases the time of transfer from preclinical to clinical study, due to requirement to study the toxicity, biodistribution, biodegradation, and clearance. That reduces the possibility of application of such nanocomposite contrast agents in clinics. Another approach to quench the fluorescence signal is to increase the concentration of the fluorescent dye, which leads to self-quenching, and as a result to decrease the fluorescence signal while increasing the photoacoustic one. An optimal candidate for this purpose is indocyanine green (ICG). ICG is an FDA-approved dye with long-time application in the clinic [18]. For self-quenching to be observable, the ICG concentration must be between 10 and 30 wt %. [19]. Several methods of ICG loading into particles have been used recently [20]. So far, no method has been put forward to encapsulate ICG within this concentration range with very high reproducibility and with the possibility of scaling up the process. Lately, we have suggested a new approach, named freezing-induced loading (FIL), that allows a very effective encapsulation [21]. The main peculiarity of this method is portionwise (quantum) loading with very high accuracy. Another advantage is the good compatibility with the LbL method [22]. Combining LbL assembly with FIL can help to obtain particles that produce both high photoacoustic and fluorescent signals. Therefore, the main goal of this work was to prepare highly efficient bimodal contrast agents and test them *in vitro*.

2. Materials and methods

2.1. Materials

Poly-L-arginine hydrochloride (PARG; Mw = 15–70 kDa) (PARG), bovine serum albumin (BSA), fetal bovine serum (FBS), phosphate buffer solution (PBS), sodium hydroxide (99.8%), ethylenediaminetetraacetic acid disodium salt (EDTA), hydrochloric acid, calcium chloride dihydrate, anhydrous sodium carbonate, sodium chloride, sodium hydroxide, and titanium dioxide were all purchased from «Sigma-Aldrich» (Germany). Dextran sulfate sodium salts (DEX; MW = 100 kDa) was purchased from Fluka (USA). Indocyanine Green was purchased from Dynamic Diagnostics (USA). Polyvinyl chloride-plastisol (PVCP) were purchased from M-F Manufacturing Co., TX (USA). All chemicals were used as received without further purification. Deionized (DI) water (specific resistivity, higher than 18.2 MΩcm) from a Milli-Q Integral 3 water purification system (Millipore) was used to make all solutions.

2.2. Methods of particle preparation

Particle preparation was divided into three main steps (Fig. 1). There were core preparation, core loading (Fig. 1(a), steps 1 and 2), core-shell and shell formation (Fig. 1(b), 3-7 steps). As a result, five types of samples were prepared (Fig. 1(c)).
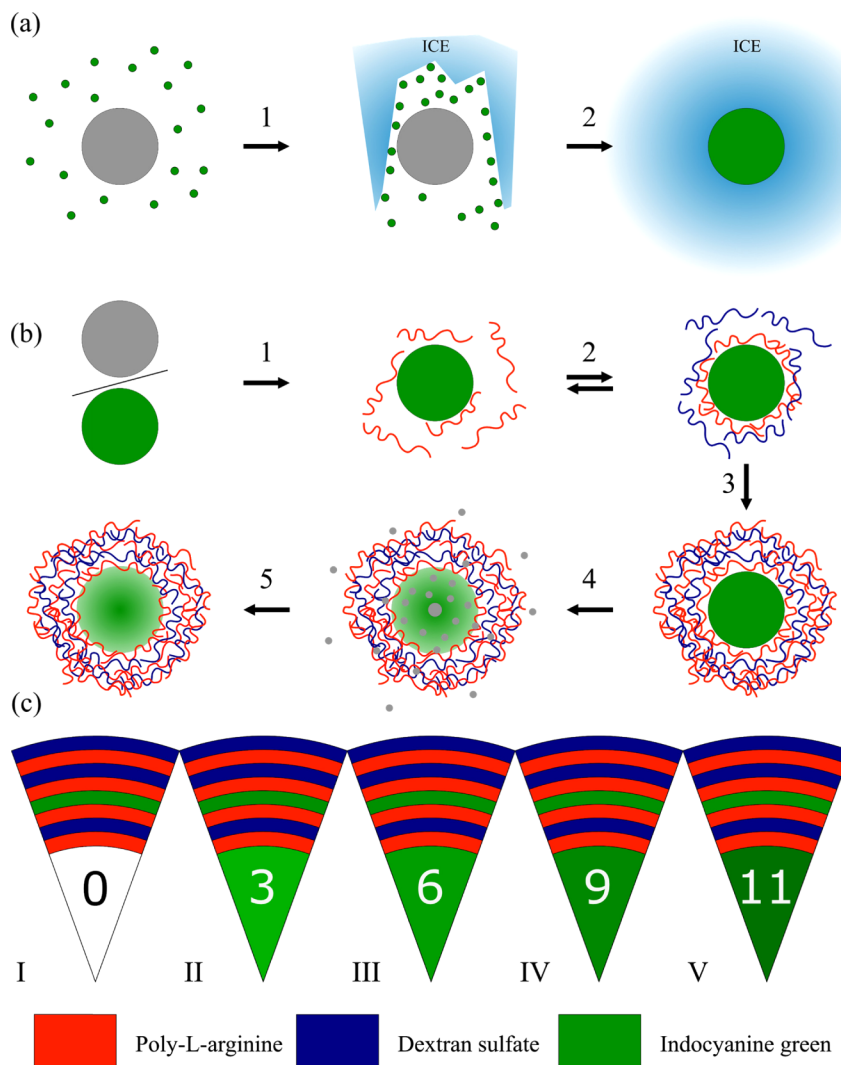
Fig. 1. Schematic representation of FIL (a) and LbL assembly (b) processes; the structures of the obtained samples (c). In part (a)step 1 is the mixing the vaterite particle suspension with the ICG&BSA solution; 2, freezing the mixture; In part (b), step 1 is adsorbing of positively charged polyelectrolyte on the surface of the vaterite core particle; 2, alternating adsorption of positively and negatively charged polyelectrolytes; 3, finishing the shell assembly with final negatively charged layer; 4, dissolving the core particle to obtain a hollow shell; 5, washing the shell after dissolving the core, the particle is ready to use. All samples have the same shell composition, but different numbers of the loading into the cores. Sample I (without loading ICG&BSA into core) and II, III, IV, V (shells) are samples with 3, 6, 9, and 11 ICG&BSA loading into cores using FIL, correspondingly.

2.2.1. Preparation of CaCO$_3$ cores

Spherical porous CaCO$_3$ cores with an average diameter of 3–6 µm were synthesized according to [23]. In brief, 2 ml of 1M CaCl$_2$ and 1M Na$_2$CO$_3$ solutions were injected into 10 ml of H$_2$O under vigorous agitation. 1 min later agitation was stopped and the resulted dispersion of particles was separated by centrifugation and washed three times with DI water.

2.2.2. Loading of CaCO$_3$ cores

Porous vaterite cores were loaded with conjugated ICG and BSA (ICG&BSA (ratio of BSA (0.8 mg/ml) to ICG (0.05 mg/ml) 16:1) by FIL (Fig. 1(a)) using 3, 6, 9, 11 freezing-thawing cycles. Also, there was the control sample of vaterite cores with no loading (0 cycles, Fig. 1(a)). ICG has a tendency of fast release from the core into the medium after loading, and the conjugation of ICG with BSA makes it harder to pass through the shell, thus avoiding the dye loss from the cores. At every FIL step, 0.5 ml of a water suspension of vaterite particles was mixed with 1.5 ml of ICG&BSA solution (Fig. 1(a), step 1) and the mixture was frozen at −20°C under constant rotation (Fig. 1(a)., step 2). Next, the mixture was thawed and the particles were sedimented by centrifugation. After centrifugation, the supernatant liquid was collected and the particles were resuspended in 0.5 ml of water. The loading cycle was then repeated.

### 2.2.3. Preparation of core–shell and shell particles

Samples were obtained by adsorption of 0.5 ml of PARG (concentration, 1 mg/ml in 0.5 M NaCl), DEX (concentration, 1 mg/ml in 0.5 M NaCl), and ICG (concentration, 0.07 mg/ml in H$_2$O) onto the spherical surfaces of the calcium carbonate cores. This was followed by the dissolving of the cores with EDTA solution (concentration 0.2 M in water, pH 7.3). LbL process consisted of several steps, that are shown in (Fig. 1(b)). The first step is adsorption of a positively charged polyelectrolyte on the core particle (step 1, Fig. 1(b)), the second step is adsorption of negatively charged polyelectrolyte on the previous layer (step 2, Fig. 1(b)). Then the adsorption process was cycled by alternating positive and negative polyelectrolytes to obtain the desired shell thickness (step 1-3, Fig. 1(b)). Instead of polyelectrolytes, one can use other charged materials, such as nanoparticles or dyes [16]. At step 6, the core of the resulting particle was dissolved to obtain hollow shells (step 4, Fig. 1(b)), that can carry substances loaded into the core particle. After each adsorption step, as well as after the dissolution of the calcium carbonate cores, the shell suspension was centrifuged and washed two times with pure water. The resulting shells (step 5, Fig. 1(b)) had structures shown in Fig. 1(c).

   Five samples of different types were prepared using a LbL deposition (Fig. 1(c)). All samples had the same shell composition, consisting of eight layers structured as follows: (PARG/DEX)(PARG/ICG)(PARG/DEX)$_2$ (Fig. 1(c). samples I–V). ICG was loaded as the fourth layer of the shell to avoid its release through the thin layers separating the dye from the surrounding medium. In contrast to samples I, samples II, III, IV and V contained different amount of ICG-labeled encapsulated BSA and were obtained as the result of a different number of freezing-induced-loading cycles – 3, 6, 9 and 11 respectively (Fig. 1(c)). Sample I was prepared by LbL deposition only [22] and samples II, III, IV, V were prepared by FIL and LbL deposition [21,22]. There are three known methods of loading (encapsulation) into particles cores—adsorption [24], coprecipitation [25] and freezing-induced-loading [21]. The latter method allows one to load a lot more material into the core comparing to others; for that reason, it was used to load the second type of particles (Fig. 1(c), samples II, III, IV and V). All samples (I-V) have a shell-only structure with the dissolved calcium carbonate cores. As a result, five samples were prepared with the following structure: Sample I: shell type ((PARG/DEX)(PARG/ICG)(PARG/DEX)$_2$; hereafter designated ICG shell); Sample II - V: shell type (from 3 up to 11 loadings of ICG-labeled BSA; shell, (PARG/DEX)(PARG/ICG)(PARG/DEX)$_2$ (hereafter designated (ICG&BSA)n/ICGshell), where n = 3, 6, 9, 11 for samples II, III, IV, V, respectively).

2.3.   Characterization of particles

2.3.1.   ICG spectra measurements

Absorption spectra of ICG were measured with an Agilent Cary 5000 UV–vis spectrometer (Agilent, USA) and ICG&BSA spectra were measured with Tecan Infinite M Nano[+] (Tecan Trading AG, Switzerland). Two ml of diluted samples were put into a plastic cuvette and placed in the spectrometer. ICG solution was diluted to concentrations of 17.5, 8.75, 4.375, 2.19, 1.09, 0.55, 0.27, 0.14, and 0.07 µg/ml. ICG&BSA solution was diluted to concentrations of 50, 25, 12.5, 6.25, 3.13, 1.56, 0.78 and 0.39 µg/ml. The obtained spectra were used to calculate calibration curves (Fig. 2). Each time ICG&BSA was loaded into the core and ICG into shell, the supernatant liquid was collected and its absorbance was measured. The results were fit into the calibration line and the concentration of ICG was calculated.
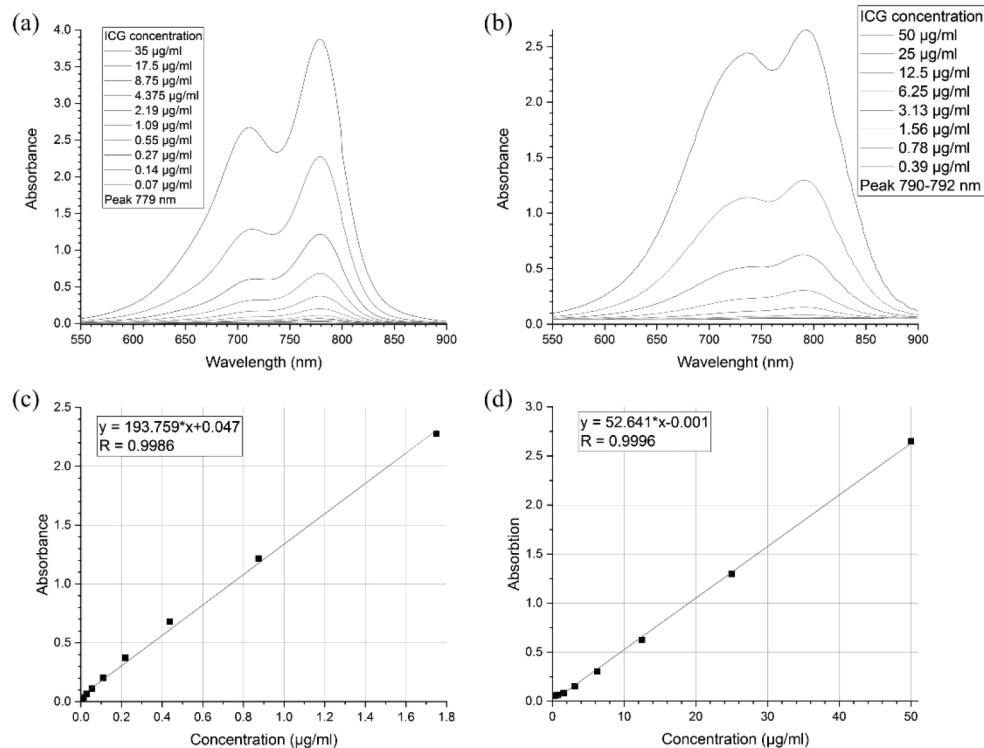
Fig. 2. Absorbance spectra and calibration curves for ICG water solution ((a) and (c)) and for aqueous ICG&BSA solution ((b) and (d)).

2.3.2.   ICG loading evaluation

Then, the mass of loaded ICG was calculated using initial ICG concentration and ICG concentration in the supernatant (Table 1). The total load is a sum of loaded masses in each load cycle.

Particle concentration was measured via CytoFLEX Flow Cytometer (Beckman Coulter). The obtained concentrations, alongside with calculated core loads, were used to estimate the load of a single particle (Table 2). The mass of ICG, loaded into the particle shell, was calculated in a similar way (Table 2).

Table 1. Calculated mass of ICG&BSA loaded into the core at every cycle loading by FIL

Load	1	2	3	4	5	6	7	8	9	10	11
Mass of loaded ICG&BSA (mg)	0.07 ±0.01	0.07 ±0.01	0.08 ±0.01	0.07 ±0.01	0.07 ±0.01	0.07 ±0.01	0.07 ±0.01	0.08 ±0.01	0.07 ±0.01	0.07 ±0.01	0.06 ±0.01

Table 2. Calculated particle concentrations and load amounts

Number of loads	0	3	6	9	11
Sample concentration, 10^6/ml	0.7± 0.1	4.4 ± 0.7	2.0 ± 0.1	4.4 ± 0.3	1.4 ± 0.1
Total amount ICG, pg/particle	1.5 ± 0.3	0.2 ± 0.03	0.5 ± 0.02	0.3 ± 0.02	1.1 ± 0.1
Shell load, pg/particle	1.5 ± 0.3	0.1 ± 0.02	0.3 ± 0.01	0.1 ± 0.01	0.5 ± 0.03

2.3.3.   DLS measurements

The measurements of the size and zeta-potential of the particles were performed using a Zetasizer Nano ZS instrument (Malvern Instruments Ltd, UK).

2.3.4.   Fluorescence imaging

Fluorescence images of shells were obtained with a Leica TCS SP8 X inverted confocal microscope (Leica Microsystems; 20× PL APO N.A. 0.7 dry objective lens).

Fluorescence signals from samples containing different ICG concentrations were measured with an IVIS Lumina XRMS In Vivo Imaging System (Xenogen Corp.), with excitation/emission at 710-760/810-875 nm. The signal was quantified with Living Image software (Xenogen Corp). All measurements were made using disposable 96 well plates at 37°C.

2.3.5.   Scanning electron microscopy

SEM was done with a JEOL JSM-7200F instrument (JEOL Ltd, Tokyo, Japan). Samples were prepared by depositing a drop of a suspension of particles on a silicon wafer and allowing it to dry at room temperature. Images were taken at 5 kV.

2.3.6.   Photoacoustic measurements

PA spectral data were recorded as described in [26]. Briefly, the sample in an acoustically coupled flow chip (μ-Slide I 0.2 Luer, hydrophobic, uncoated, IBIDI, Germany) was illuminated by nanosecond pulsed excitation light from an optical parametric oscillator (OPO) laser (Spitlight-DPSS 250 ZHG-OPO, Innolas, Germany) running at a repetition rate of 50 Hz. The acoustic signals were recorded by a cylindrically focused single-element transducer (V382-SU, 3.5 MHz, Olympus, Germany). The sample OA intensity is given in reference to a solution of naphtol blue-black.

2.3.7.   FLIM measurements

For testing the hypothesis of impact of ICG concentration on fluorescent properties of capsules the fluorescent lifetime imaging (FLIM) was performed with the Microtime 200 setup (PicoQuant, Germany) with picosecond 638 nm excitation (40 MHz repetition rate, maximum power 50 μW, pulse duration = 40 ps). Imaging was performed with a 100× 1.4NA objective (Olympus UPlanSApo), image size was 400×400 pixels with a collection time of 0.2 ms/pixel, i.e. collection

time for the whole 80×80 µm image was 40 s. Detection was performed in one spectral channel 690 ± 35 nm. Fluorescence decay kinetics were acquired using time-correlated single photon counting method and processed using the custom-made software written in Python programming language. The binning value was set to 4 (i.e. fluorescence signal was averaged over 81 pixels), and only the fluorescence decay profiles with ≥ 100 photon counts in maximum were analysed. Fluorescence decay curves were fitted with two exponential terms with respect to IRF. Amplitudes (a_1, a_2) and decay lifetimes (τ_1, τ_2) were used to calculate mean lifetime as $\tau_{mean} = (a_1\tau_1 + a_2\tau_2)/(a_1 + a_2)$. We should note that the excitation wavelength does not correspond to the maximum of the absorption band of indocyanine green, and the spectral range of detection captures the fluorescence emission, which partially overlaps with absorption, however, an intense fluorescent response was observed in all FLIM images localized in the capsules under study. Samples with the following number of protein conjugate loadings inside the capsules that also contained indocyanine in the shell structure were studied: 0, 3, 6, 9, 11.

3. Results

Figure 3 shows the fluorescence signals as a function of the ICG concentration in ICG&BSA conjugate solution and in the free ICG solution. The fluorescence signals are increasing with ICG concentration in the low-concentration region (<0.02 mg/ml), then it has a maximum and finally starts to decrease with the growing concentration (Fig. 3). Thus, one can say that a quenching effect had taken place for both indocyanine green and indocyanine green conjugated with BSA (Fig. 3). ICG conjugated with BSA gave stronger signal and at the same time the maximum of fluorescence dependence on concentration was shifted to lower values, compared to the free ICG (Fig. 3(b)).
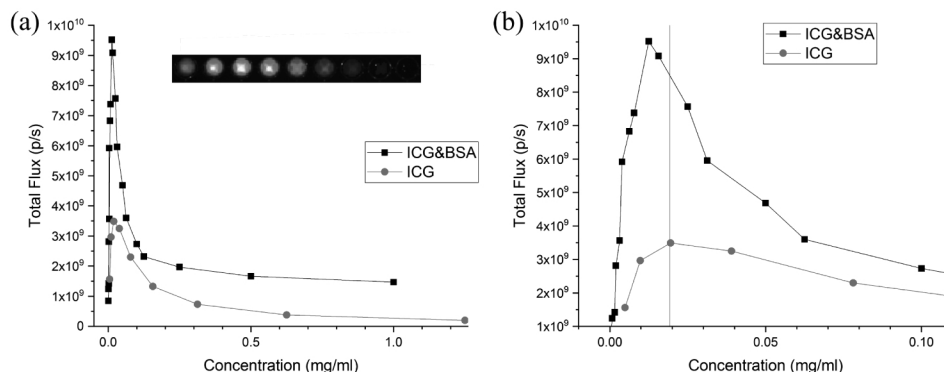

Fig. 3. The fluorescence signals versus the ICG concentration (a, b). Red colour marks the fluorescence signal of ICG solution. Black colour marks the fluorescence signal of ICG&BSA conjugate. The insert shows fluorescence imaging of a plate with nine ICG concentrations used in the plot. Panel (b) shows the shifting of peak at smaller concentrations. Vertical red line represents value of ICG concentration at maximum fluorescence.

Figure 4 demonstrated the absorbance and optoacoustic spectra (a) at difference ICG concentration. Increasing of ICG concentration led to increasing of both optoacoustic and absorbance signals (Fig. 4(b)). The ICG concentration was varied in the interval including the concentrations at maximum fluorescence and self quenching effect observation (Fig. 3). SEM images (Fig. 5) of sample V demonstrated that cores are successfully dissolved and as a result, the hollow capsules - shells have been prepared.
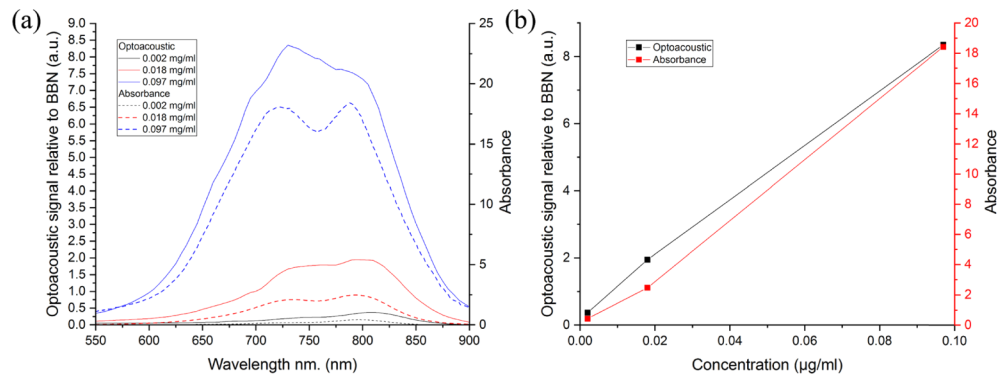
Fig. 4. Absorbance and optoacoustic spectra (a) and absorbance and optoacoustic signals (b) at wavelength 800 nm on ICG concentration dispersed in 10% fetal bovine serum aqueous solution.
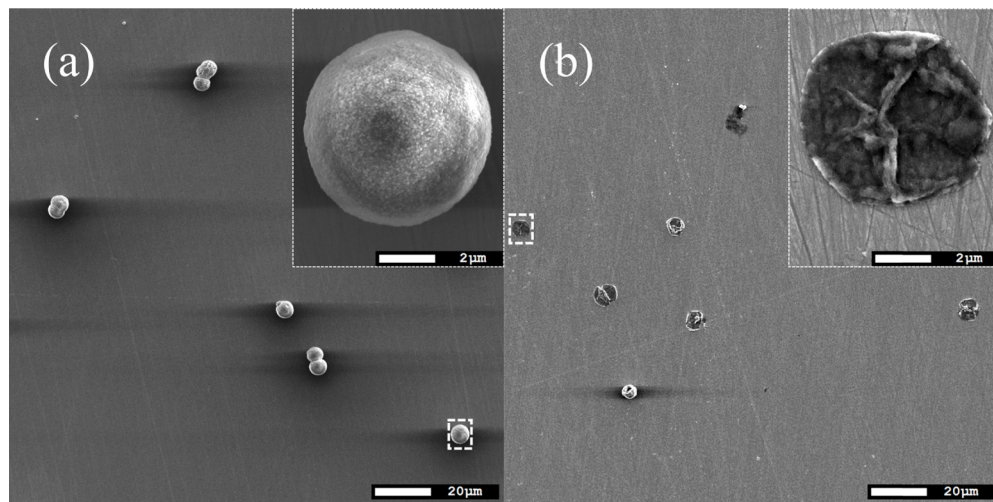
Fig. 5. SEM images of sample (ICG&BSA)11/ICGshell before(a) and after(a) dissolution of the core.

Confocal fluorescence microscopy images of ICGshell, (ICG&BSA)6/ICGshell and (ICG&BSA)11/ICGshell are presented in Fig. 6(a–f). It is clearly seen that all samples give a fluorescent signal (Fig. 6(a,b,c)). The transmission bright field images demonstrated that cores were fully dissolved and most of the shells had a spherical shape (Fig. 6(d,e,f)). All images (Fig. 6(a–f)) were obtained at the same sensitivity settings of CLSM.

The absorbance spectra of ICG solution samples with different dye concentration are shown in Fig. 2(a). All spectra have two peaks (at 779 and 711 nm), in good agreement with the previous studies [18,19,27–29]. The calibration line in Fig. 2(c) was based on the peak values of each spectrum, each peak value corresponding to a certain ICG concentration (Fig. 2(e)). The absorbance spectra for ICG&BSA are shown in Fig. 2(b). For each sample concentration, the first peak shifts to larger wavelengths with increasing concentration, from 790 nm at 0.39 μ/ml to 792 nm at 50 μ/ml. The second peak shifts from 738 nm at 50 μg/ml to 742 nm at 0.39 μg/ml with decreasing concentration until it cannot be distinguished as a peak, starting with the concentration of 12.5 μg/ml. These results correspond to those from the previous studies [18,21]. The shift is caused by the conjugation of ICG to BSA. ICG is known to bind strongly to serum
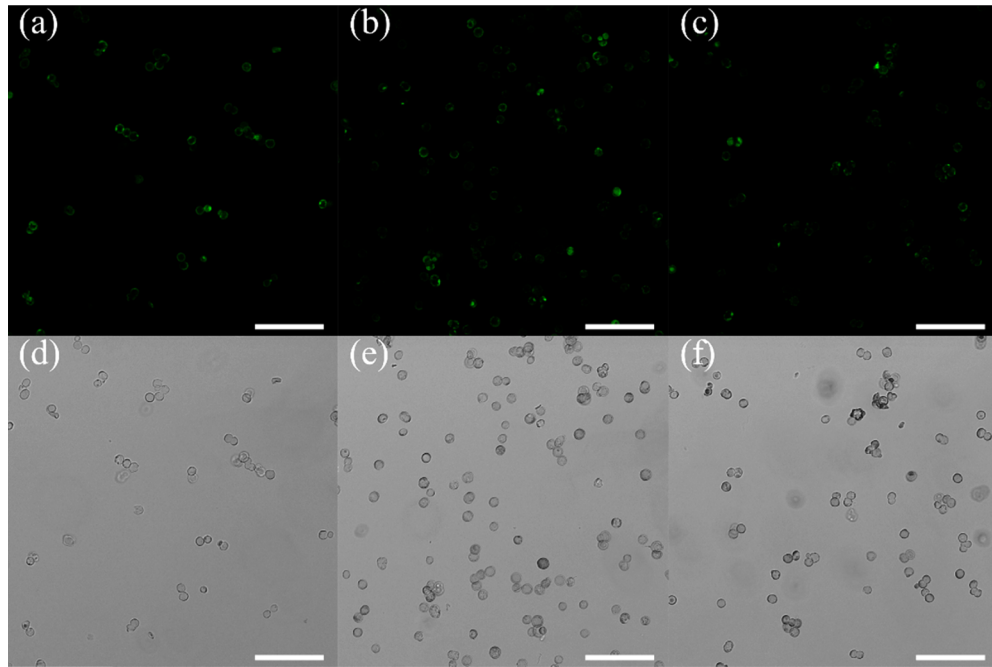
Fig. 6. Confocal fluorescence microscopy images (a, b, c) and transmission bright field (d, e, f) images of ICGshell, (ICG&BSA)6/ICGshell and (ICG&BSA)11/ICGshell. The scale bar is 50 μm.

albumin [30,31]. The obtained data were used to calculate the loaded ICG mass per particle per each FIL cycle (Table 1 and Table 2). The total load of 0.79 mg (about 0.07 mg per freezing cycle, Table 1) correlates well with the previous study [22]. The particle concentration was measured with a CytoFLEX S Flow Cytometer (Beckman Coulter) and the results are shown in Table 2.

The measurements of the size and zeta-potential of the particles were performed using a Zetasizer Nano ZS instrument (Malvern Instruments Ltd, UK) and data are presented in Table 3. Magnitude of Zeta potential of particle is determined by amount of ICG in the shell and maximum is obtained for ICG shell (Table 3). The size of particle does not practically depend on loading number within the measurement uncertainty interval (Table 3). The exception is sample with 11 loadings where the size is bigger than size for other samples. It can be explained by osmotic pressure for this sample because of the highest amount of ICG&BSA conjugate has been encapsulated (Table 4).
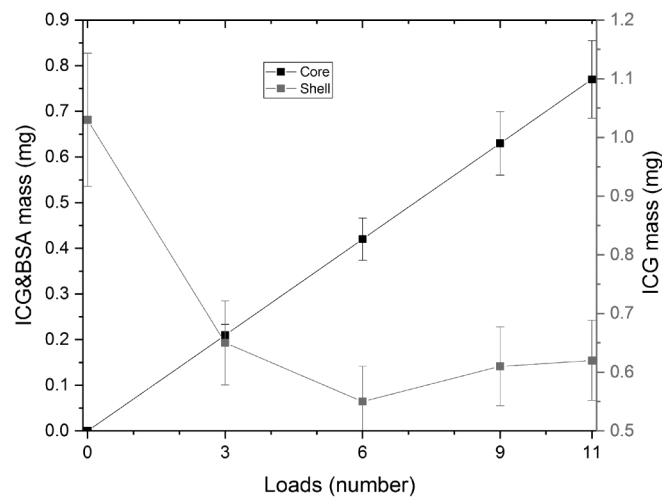
Table 3. Measured particle size and zeta potentials

Number of loads	0	3	6	9	11
Size, μm	5 ± 1	5 ± 1	4.4 ± 0.4	3.4 ± 0.3	7 ± 1
Zeta potential, mV	-32 ± 6	-36 ± 15	-26 ± 7	-22 ± 12	-23 ± 8

The tendency of ICG&BSA and ICG loading to the core and shell of the particles is shown in Fig. 7 and Table 4. It is seen that the tendency of loading of ICG&BSA into the core is linear. One can also see that the amount of ICG loaded into the shell is decreasing with the increasing number of ICG&BSA loadings into the core.

Table 4. Measured amount of ICG loaded into particle core and shell

Number of loads	ICG&BSA mass loaded into the core (mg)	ICG mass loaded into the shell (mg)	Total loaded mass of dye (mg)	Mass fraction of dye in the shell
0	0	1.03	1.03	100%
3	0.22	0.65	0.87	75%
6	0.43	0.55	0.98	56%
9	0.65	0.61	1.26	48%
11	0.79	0.62	1.41	44%

Fig. 7. The comparison of ICG&BSA and ICG to the particles core and shell respectively.

When ICG was being loaded into the shell, we noticed that the dye molecules adsorbed on the particles without load better than on loaded particles. This phenomenon is shown in Fig. 8. The dye is affected by the concentration gradient and electrostatic force, which attracts or repels the molecules, depending on the core's content. ICG in solution is charged negatively and is attracted to a positively charged polyelectrolyte layer of the shell. Because the ICG shell sample (Fig. 8(a)) has no dye in its core, it creates a concentration gradient directed from the core. This gradient causes diffusion toward the core, thereby increasing the amount of loaded ICG. Both forces increase the adsorption of ICG in the shell, which results in a larger amount of ICG in the shell. In (ICG&BSA)n/ICGshell samples (Fig. 8(b)), the high concentration of ICG inside the core creates the overall negative charge, which repels ICG from the shell and creates a concentration gradient directed into the core, with subsequent diffusion outwards from the core. The resulting effect on ICG in solution is the decreasing adsorption to the shell. This phenomenon was observed before [16].

Figure 9 shows typical FLIM images of capsules and histograms of mean lifetime distribution, weighted by the integral pixel intensity. As can be seen, fluorescence mean lifetime values shifts to values of the order of 0.2 ns, which corresponds to the decay time of ICG fluorescence in water, where it is in the quenched state. In the Fig. 9(e) one can see the trend of fluorescence mean
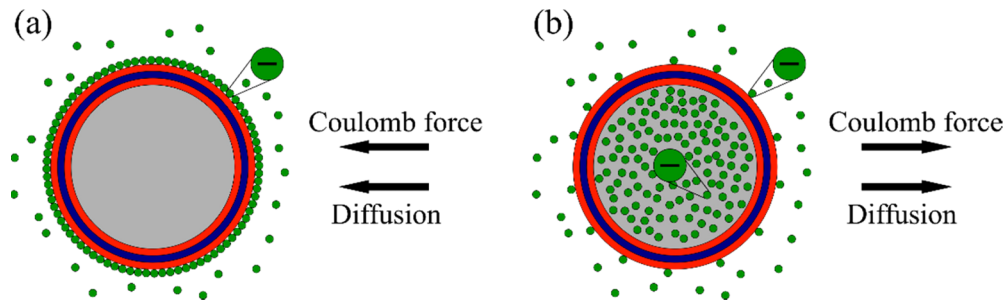
Fig. 8. Schematic representation of loading of ICG into the core without load (a) and into loaded core (b).

lifetime to decrease with increasing the number of core loads, which is typical for the quenching effect [32].

The PA and absorbance spectra of particles are shown in Fig. 10. As one can see, PA signal is proportional to absorbance. Besides, the peaks of both PA and absorbance signals start at about 625 nm and end at about 875 nm. This range lies within biological tissue transparency window [33].

Figure 10(b) shows PA and fluorescence signals dependencies of capsules on amount of ICG&BSA conjugate loaded into particles core. It can be seen that ICG shell (i.e. the particles without the core loadings) gave the highest photoacoustic signals. It is common that PA signal is proportional to the concentration of PA signalling compound. In Fig. 10(b) PA signal of particles is in correlation with the amount of dye in the particles shell. For samples (ICG&BSA)9/ICGshell and (ICG&BSA)11/ICGshell, one can observe deviations from that tendency. That phenomenon can be described in the following way. The PA signals are mainly produced by the shell and that means the more dye absorbed to the shell, the larger the PA signals will be. The curves (Fig. 10(a, b)) are in a good agreement with the calculated shell load. The deviations of the last two samples are possibly due to the fact that with increasing concentration of conjugate, probability of absorption of that conjugate to the inner layer of the shell is increased. This increases the amount of dye in the shell but at the same time increases the thickness of the shell, which is decreasing the PA signal from the shell.
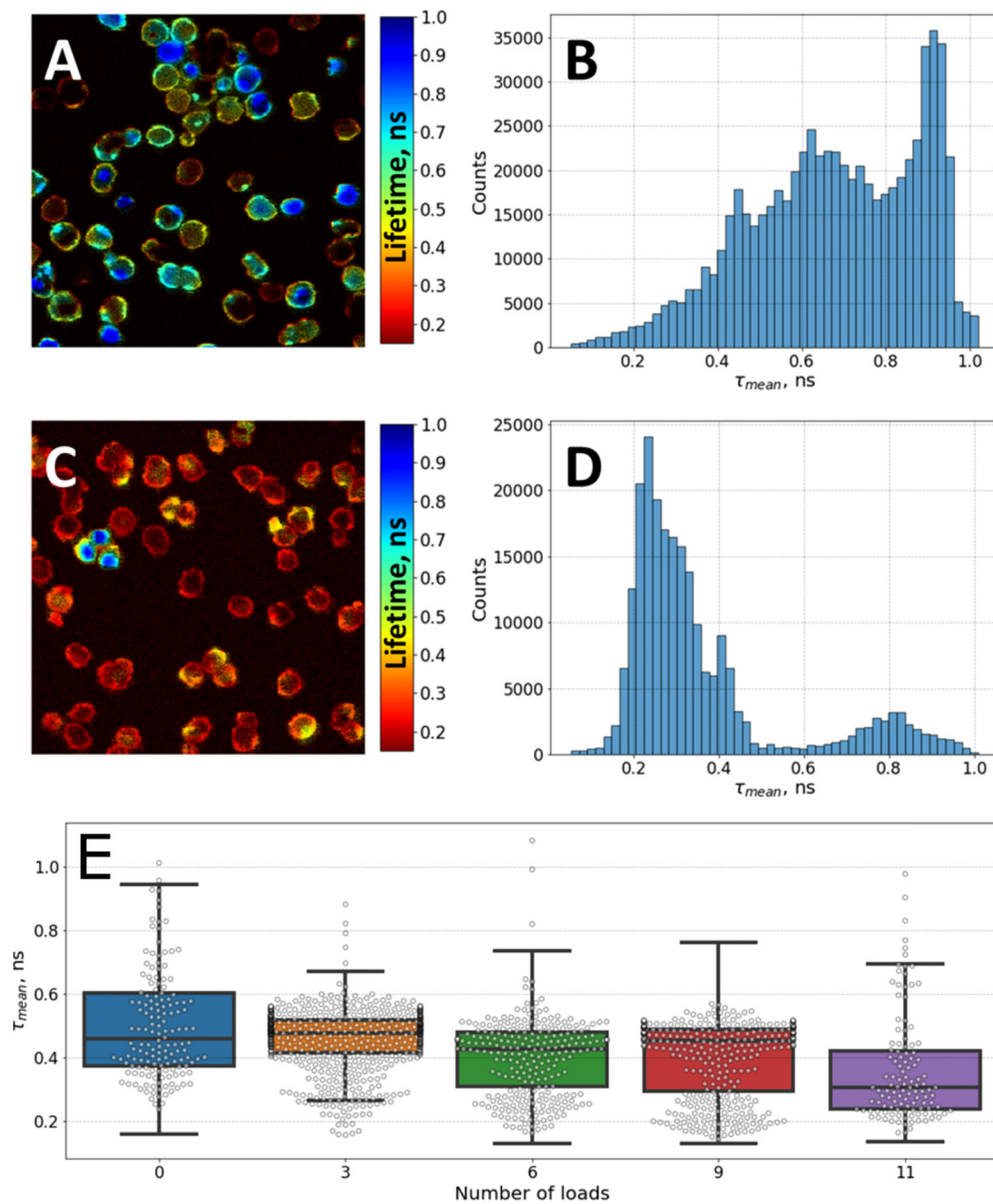
Fig. 9. (A, C) - FLIM images of capsules with 0 and 11 loads; (B, D) - histograms of the distribution of the mean lifetime for samples with 0 and 11 loads. (E) - Mean fluorescence lifetime in samples with different number of loads
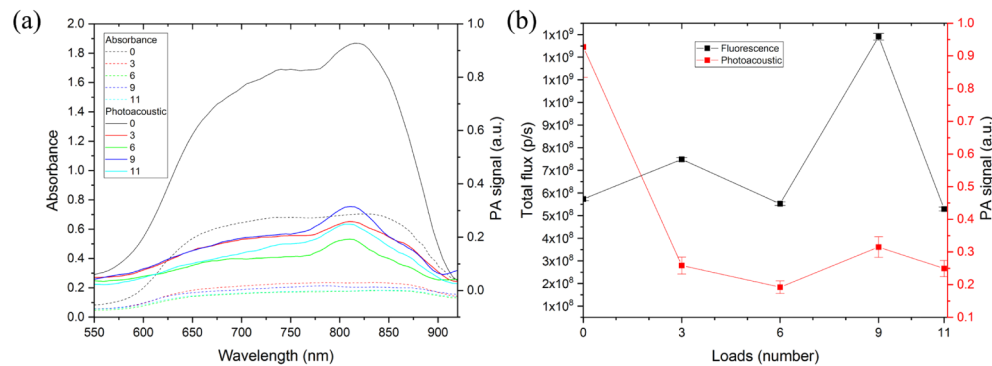
Fig. 10. The comparison of absorbance and photoacoustic spectra of particles with a different number of loads (a) and the fluorescence and photoacoustic signals of particles as a function of the number of loads of ICG&BSA into particles core (b). All particles had the same concentration of $0.7 \cdot 10^6$/ml.

4.   Conclusions

A new type of organic dye/polymer particles, with both PA(OA) and fluorescent properties, was made by combining layer-by-layer assembly with freezing-induced loading. FIL method was used to obtain a high local ICG concentration, that is required for the self-quenching effect. By this means, it became possible to significantly increase the PA signals. At the same time, the presence of the ICG molecules in the shell embedded by LbL assembly ensure an acceptable level of the fluorescence signal. When ICG was being loaded into the shell, it was noticed that the dye molecules adsorbed on particles without load better than on loaded particles. It was due to the concentration gradient of ICG and to the Coulomb interaction (repulsion) between the ICG being adsorbed and the core loaded with ICG-protein conjugates. The prepared ICG/polymer particles demonstrated significant PA and fluorescence signal levels in the biological tissue transparency window. The PA signal of particles is in correlation with the amount of dye in the particles shell because the PA signals are mainly produced by the shell. Increasing of ICG concentration in the shell led the PA signal growing. The developed type of particles holds good promise as a next-generation of multifunctional drug delivery carriers with combined functionalities such as (1) usability in PA(OA) and fluorescence tomography imaging and in organic-dye-based photodynamic therapy and (2) high biocompatibility and biodegradability.

Funding

Acknowledgements

Disclosures

The authors declare that there are no conflicts of interest related to this article.

References

1. D. Zhang, M. Wu, Y. Zeng, N. Liao, Z. Cai, G. Liu, X. Liu, and J. Liu, "Lipid micelles packaged with semiconducting polymer dots as simultaneous MRI/photoacoustic imaging and photodynamic/photothermal dual-modal therapeutic agents for liver cancer," J. Mater. Chem. B **4**(4), 589–599 (2016).

2. N. Beziere, N. Lozano, A. Nunes, J. Salichs, D. Queiros, K. Kostarelos, and V. Ntziachristos, "Dynamic imaging of PEGylated indocyanine green (ICG) liposomes within the tumor microenvironment using multi-spectral optoacoustic tomography (MSOT)," Biomaterials **37**, 415–424 (2015).

3. K. C. Wei, P. C. Chu, H. Y. J. Wang, C. Y. Huang, P. Y. Chen, H. C. Tsai, Y. J. Lu, P. Y. Lee, I. C. Tseng, L. Y. Feng, P. W. Hsu, T. C. Yen, and H. L. Liu, "Focused Ultrasound-Induced Blood-Brain Barrier Opening to Enhance Temozolomide Delivery for Glioblastoma Treatment: A Preclinical Study," PLoS One **8**(3), e58995 (2013).

4. P. K. Morrish, G. V. Sawle, and D. J. Brooks, "An [18F]dopa-PET and clinical study of the rate of progression in Parkinson's disease," Brain **119**(2), 585–591 (1996).

5. G. Savelli, A. Chiti, G. Grasselli, M. Maccauro, M. Rodari, and E. Bombardieri, "The Role of Bone SPET Study in Diagnosis of Single Vertebral Metastases," Anticancer Res. **20**(2 B), 1115–1120 (2000).

6. V. Ntziachristos, C. H. Tung, C. Bremer, and R. Weissleder, "Fluorescence molecular tomography resolves protease activity in vivo," Nat. Med. **8**(7), 757–761 (2002).

7. C. Lee, S. Han, S. Kim, M. Jeon, M. Y. Jeon, C. Kim, and J. Kim, "Combined photoacoustic and optical coherence tomography using a single near-infrared supercontinuum laser source," Appl. Opt. **52**(9), 1824 (2013).

8. A. S. Timin, M. M. Litvak, D. A. Gorin, E. N. Atochina-Vasserman, D. N. Atochin, and G. B. Sukhorukov, "Cell-Based Drug Delivery and Use of Nano-and Microcarriers for Cell Functionalization," Adv. Healthcare Mater. **7**(3), 1700818 (2018).

9. K. A. Kang, J. Wang, J. B. Jasinski, and S. Achilefu, "Fluorescence Manipulation by Gold Nanoparticles: From Complete Quenching to Extensive Enhancement," J. Nanobiotechnol. **9**(1), 16 (2011).

10. G. Schneider, G. Decher, N. Nerambourg, R. Praho, M. H. V. Werts, and M. Blanchard-Desce, "Distance-dependent fluorescence quenching on gold nanoparticles ensheathed with layer-by-layer assembled polyelectrolytes," Nano Lett. **6**(3), 530–536 (2006).

11. S. T. Sivapalan, J. H. Vella, T. K. Yang, M. J. Dalton, R. N. Swiger, J. E. Haley, T. M. Cooper, A. M. Urbas, L. S. Tan, and C. J. Murphy, "Plasmonic enhancement of the two photon absorption cross section of an organic chromophore using polyelectrolyte-coated gold nanorods," Langmuir **28**(24), 9147–9154 (2012).

12. R. Bardhan, N. K. Grady, J. R. Cole, A. Joshi, and N. J. Halas, "Fluorescence Enhancement by Au Nanostructures: Nanoshells and Nanorods," ACS Nano **3**(3), 744–752 (2009).

13. E. S. Prikhozhdenko, D. N. Bratashov, V. S. Atkin, R. A. Kamyshinsky, A. L. Vasiliev, B. N. Khlebtsov, D. A. Gorin, H. Möhwald, and A. M. Yashchenok, "Precise control of distance between plasmonic surface-enhanced Raman scattering substrate and analyte molecules with polyelectrolyte layers," J. Raman Spectrosc. **49**(10), 1581–1593 (2018).

14. H. Kuhn, "Functionalized monolayer assembly manipulation," Thin Solid Films **99**(1-3), 1–16 (1983).

15. H. Bücher, K. H. Drexhage, M. Fleck, H. Kuhn, D. Möbius, F. P. Schäfer, J. Sondermann, W. Sperling, P. Tillmann, and J. Wiegand, "Controlled Transfer of Excitation Energy Through Thin Layers," Mol. Cryst. **2**(3), 199–230 (1967).

16. M. V. Novoselova, D. N. Bratashov, M. Sarimollaoglu, D. A. Nedosekin, W. Harrington, A. Watts, M. Han, B. N. Khlebtsov, E. I. Galanzha, D. A. Gorin, and V. P. Zharov, "Photoacoustic and fluorescent effects in multilayer plasmon-dye interfaces," J. Biophotonics **12**(4), e201800265 (2019).

17. C. Yu, S. Wu, and W. Tseng, "Magnetite Nanoparticle-Induced Fluorescence Quenching of Adenosine Triphosphate – BODIPY Conjugates: Application to Adenosine Triphosphate and Pyrophosphate Sensing," Anal. Chem. **85**(18), 8559–8565 (2013).

18. J. T. Alander, I. Kaartinen, A. Laakso, T. Pätilä, T. Spillmann, V. V. Tuchin, M. Venermo, and P. Välisuo, "A Review of Indocyanine Green Fluorescent Imaging in Surgery," Int. J. Biomed. Imaging **2012**, 1–26 (2012).

19. V. J. Pansare, W. J. Faenza, H. Lu, D. H. Adamson, and R. K. Prud'homme, "Formulation of long-wavelength indocyanine green nanocarriers," J. Biomed. Opt. **22**(09), 1 (2017).

20. Z. Sheng, D. Hu, M. Xue, M. He, P. Gong, and L. Cai, "Indocyanine Green Nanoparticles for Theranostic Applications," Nano-Micro Lett. **5**(3), 145–150 (2013).

21. S. V. German, M. V. Novoselova, D. N. Bratashov, P. A. Demina, V. S. Atkin, D. V. Voronin, B. N. Khlebtsov, B. V. Parakhonskiy, G. B. Sukhorukov, and D. A. Gorin, "High-efficiency freezing-induced loading of inorganic nanoparticles and proteins into micron- and submicron-sized porous particles," Sci. Rep. **8**(1), 17763 (2018).

22. G. Decher, J. D. Hong, and J. Schmitt, "Buildup of ultrathin multilayer films by a self-assembly process : III . Consecutively alternating adsorption of anionic and cationic polyelectrolytes on charged surfaces," Thin Solid Films **210-211**, 831–835 (1992).

23. D. V. Volodkin, A. I. Petrov, M. Prevot, and G. B. Sukhorukov, "Matrix Polyelectrolyte Microcapsules: New System for Macromolecule Encapsulation," Langmuir **20**(8), 3398–3406 (2004).

24. Y. I. Svenskaya, H. Fattah, A. M. Zakharevich, D. A. Gorin, G. B. Sukhorukov, and B. V. Parakhonskiy, "Ultrasonically assisted fabrication of vaterite submicron-sized carriers," Adv. Powder Technol. **27**(2), 618–624 (2016).

25. Y. I. Svenskaya, A. M. Pavlov, D. A. Gorin, D. J. Gould, B. V. Parakhonskiy, and G. B. Sukhorukov, "Photodynamic therapy platform based on localized delivery of photosensitizer by vaterite submicron particles," Colloids Surf., B **146**, 171–179 (2016).

26. P. Vetschera, K. Mishra, J. P. Fuenzalida-Werner, A. Chmyrov, V. Ntziachristos, and A. C. Stiel, "Characterization of Reversibly Switchable Fluorescent Proteins in Optoacoustic Imaging," Anal. Chem. **90**(17), 10527–10535 (2018).

27. K. Urbanska, B. Romanowska-Dixon, Z. Matuszak, J. Oszajca, P. Nowak-sliwinska, and G. Stochel, "Indocyanine green as a prospective sensitizer for photodynamic therapy of melanomas Indocyanine green as a prospective sensitizer for photodynamic therapy of melanomas," Acta Biochim. Pol. **49**(2), 387–391 (2002).

28. J. F. Zhou, M. P. Chin, and S. A. Schafer, "Aggregation and degradation of indocyanine green," Proc. SPIE **2128**, 495–505 (1994).

29. M. L. J. Landsman, G. Kwant, C. Physiology, G. A. Mook, and W. G. Zijlstra, "Light-absorbing properties, stability, spectral stabilization of indocyanine green," J. Appl. Physiol. **40**(4), 575–583 (1976).

30. Z. Sheng, D. Hu, M. Zheng, P. Zhao, H. Liu, P. Gong, G. Gao, P. Zhang, and L. Cai, "Smart Human Serum Albumin-Indocyanine Green Nanoparticles Generated by Programmed Assembly for Dual-Modal Imaging-Guided Cancer Synergistic Phototherapy," ACS Nano **8**(12), 12310–12322 (2014).

31. A. Sahu, J. Hyun, H. Gyeong, Y. Yeon, and G. Tae, "Prussian blue / serum albumin / indocyanine green as a multifunctional nanotheranostic agent for bimodal imaging guided laser mediated combinatorial phototherapy," J. Controlled Release **236**, 90–99 (2016).

32. J. R. Lakowicz, ed., *Principles of Fluorescence Spectroscopy*, 3rd ed. (Springer US, 2006).

33. V. V. Tuchin, *Tissue Optics : Light Scattering Methods and Instruments for Medical Diagnosis*, 3rd ed. (SPIE Press, 2015).